The Astrophysical Journal, 653:835–842, 2006 December 20

THE COSMIC MICROWAVE BACKGROUND TEMPERATURE AND GALACTIC EMISSION AT 8.0 AND 8.3 GHz

J. Singal,[1,2] D. J. Fixsen,[3] A. Kogut,[4] S. Levin,[5] M. Limon,[3] P. Lubin,[1]
P. Mirel,[3] M. Seiffert,[5] and E. J. Wollack[4]
Received 2006 June 22; accepted 2006 August 31

ABSTRACT

We report balloon-borne measurements at 8.0 and 8.3 GHz of Galactic emission and of the radiometric temperature of the cosmic microwave background, the results from the first flight of the ARCADE 2 (Absolute Radiometer for Cosmology, Astrophysics, and Diffuse Emission) instrument. We find the Galactic free-free emission intensity in the plane to be two-thirds as high as that predicted by a naive extrapolation of 2003 *WMAP* K-band data, a result consistent with 2006 *WMAP* findings, and find the Galactic synchrotron emission intensity to be approximately as high as that predicted by a naive interpolation of Haslam all-sky survey and *WMAP* K-band data. We find $T_{\rm CMB}$ to be 2.90 ± 0.12 K at 8.0 GHz and 2.77 ± 0.16 K at 8.3 GHz.

Subject headings: cosmic microwave background — Galaxy: general — instrumentation: detectors

1. INTRODUCTION

The measurement of cosmic microwave background (CMB) temperature and Galactic emission reported here, at 8.0 and 8.3 GHz, is the first of the second-generation Absolute Radiometer for Cosmology, Astrophysics, and Diffuse Emission (ARCADE 2) experiment, which is a balloon-borne instrument designed to measure the radiometric temperature of the sky at a range of frequencies from 3 to 90 GHz.

The primary science goal of the ARCADE project is to measure the frequency spectrum of the CMB at long wavelengths. The shape of this spectrum can provide powerful constraints on the energetics of the early universe. The CMB has been shown by the Far-Infrared Absolute Spectrophotometry (FIRAS) instrument to be a nearly ideal blackbody spectrum from ~60 to ~600 GHz, with a temperature of 2.725 ± 0.001 K (Fixsen et al. 1996). At lower frequencies, however, existing measurements have uncertainties ranging from 10 mK at 10 GHz to 140 mK at 2 GHz (see Fixsen et al. 2004 for a recent review). Figure 1 shows existing low-frequency CMB temperature measurements and their uncertainties. The CMB spectrum is expected to deviate from that of a blackbody below the frequencies measured by FIRAS.

A distortion of the CMB spectrum below 10 GHz is expected as a result of free-free emission from thermal bremsstrahlung in galactic halos and the intergalactic medium. The change in CMB temperature is given by

$$\Delta T_{\rm ff} = T_{\gamma,0}\,\frac{Y_{\rm ff}}{x^2},$$

where x is the dimensionless frequency $x = h\nu/kT_{\gamma,0}$ and $Y_{\rm ff}$ is the optical depth to free-free emission, given by

$$Y_{\rm ff} = \int_{t_{\rm max}}^{t_0} \frac{T_e - T_\gamma}{T_e}\,\frac{8\pi e^6 h^2 n_e^2 g}{3m_e(kT_{\gamma,0})^3\sqrt{6\pi m_e kT_e}}\,dt'.$$

Here T_e and T_γ are the electron and photon temperatures, respectively, t is time, with a subscript zero designating the present, n_e is the free electron number density, m_e is the electron mass, h is Planck's constant, and g is the Gaunt factor (Bartlett & Stebbins 1991). A cosmological free-free signal is thus characterized by a quadratic rise in the CMB temperature at long wavelengths. A measurement of such a distortion, and therefore the free-free optical depth, is a measurement of the integrated amount of ionization looking back. This would place a powerful constraint on the era of luminous-object formation or the extent of electron clumping in galactic halos. The current constraint on $Y_{\rm ff}$, from ground-based measurements at 2 GHz, is $Y_{\rm ff} < 2 \times 10^{-5}$, corresponding to a distortion of $\Delta T < 19$ mK at 3 GHz (Bersanelli et al. 1994).

Another CMB spectral distortion mechanism is the possible decay of relic particles in the early universe. An injection of energy into the baryon or photon component of the universe from a component previously decoupled from it would be preserved as a distortion to the photon spectrum. For energy injections before a thermalization redshift of $z_{\rm therm} \approx 10^4$ and after a redshift of $z_{\rm max} \approx 10^6$, the photon spectrum will achieve thermal equilibrium with the electrons through scattering events. Since the timescale for chemical equilibrium through particle creation events is much longer, the resulting photon spectrum will be that of an equilibrium Bose-Einstein distribution with a nonzero chemical potential μ (Burigana et al. 1991; Zel'dovich & Sunyaev 1969). As the injected energy at such an early time would presumably be from dark matter decays, a measurement of μ could constrain the mass, lifetime, and abundance of such particles.

The ARCADE observations also provide information on microwave emission from our Galaxy. Galactic emission at the ARCADE 2 frequencies is less well characterized than the CMB spectrum, with a gap in full-sky coverage measurements between the lowest *Wilkinson Microwave Anisotropy Probe* (*WMAP*) observing band, at 23 GHz (Bennett et al. 2003), and the Haslam all-sky survey at 408 MHz (Haslam et al. 1982). Surveys covering at least half of the sky in the intervening frequencies have been carried out at 1.42 GHz (Reich 1982; Reich & Reich 1986; Reich et al. 2001) and 2.326 GHz (Jonas et al. 1998).

Emission from the Milky Way at frequencies below 20 GHz is dominated by free-free and synchrotron radiation, with the synchrotron component increasingly dominant at lower frequencies. Synchrotron emission results from cosmic-ray electrons accelerated in the Galactic magnetic field. Its frequency dependence

[1] Department of Physics, University of California, Santa Barbara, Santa Barbara, CA 93106-9530.
[2] Current address: Observational Cosmology Laboratory, Code 665, NASA Goddard Space Flight Center, Greenbelt, MD 20771.
[3] Science Systems and Applications, Inc., Code 665, NASA Goddard Space Flight Center, Greenbelt, MD 20771.
[4] Astrophysics Science Division, Code 665, NASA Goddard Space Flight Center, Greenbelt, MD 20771.
[5] Jet Propulsion Laboratory, California Institute of Technology, 4800 Oak Drive, Pasadena, CA 91109.

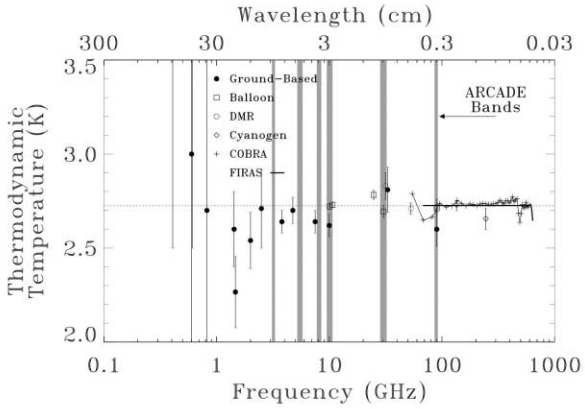

FIG. 1.—Existing low-frequency CMB temperature measurements and their uncertainties. Adopted from Fixsen et al. (2004).

may be approximated as a power law $T \sim \nu^{\beta}$, with spectral index $\beta = -2.8$ between 408 MHz and 20 GHz and steepening to -3.3 above 40 GHz (Platania et al. 1998; Bennett et al. 2003). The synchrotron spectral index varies across the sky and is steeper at the poles than in the Galactic plane (Reich & Reich 1988; Bennett et al. 2003). Free-free emission results from thermal bremsstrahlung in ionized regions of the Galaxy. It follows a power-law spectral index of -2.1. Since it tracks heavily ionized regions, free-free emission is more concentrated toward the Galactic plane than is synchrotron emission.

A possible additional component of Galactic microwave emission is from spinning dust, which has a peak in intensity between 20 and 40 GHz, cutting off sharply at the high and low ends (Draine & Lazarian 1998). ARCADE 2 measurements can therefore potentially distinguish between spinning-dust emission and constant-spectrum free-free and synchrotron.

As designed, the ARCADE 2 instrument can perform a doubly nulled measurement, where the radiometric temperature of the sky is compared with that from an external calibrator, with the radiometer itself containing a nulling internal reference load. In this way, input to the first-stage amplifier is switched between the sky horn and the internal reference load, while the external calibrator allows the horn to alternately view either the sky or a known blackbody. The external calibrator target is at least 40 dB and as much as 68 dB black in the frequency range from 3 to 90 GHz (Fixsen et al. 2006). By comparison with the external calibrator, errors in the determination of the sky temperature resulting from systematic effects in the radiometer chain can be eliminated to first order.

This paper describes measurements from the first flight of the instrument, where because of a drive-system failure we were only able to view the sky at one frequency band and were unable to utilize the external calibrator. The results presented are thus limited by the systematic effects of not having an external calibrator, resulting in a measurement of $T_{\rm CMB}$ that is much less constrained than future measurements with ARCADE 2 will be. The determination of Galactic structure, however, is much less dependent on these systematic effects.

2. THE INSTRUMENT

To achieve precise absolute temperature measurements of the sky, the ARCADE 2 instrument features a novel design using an

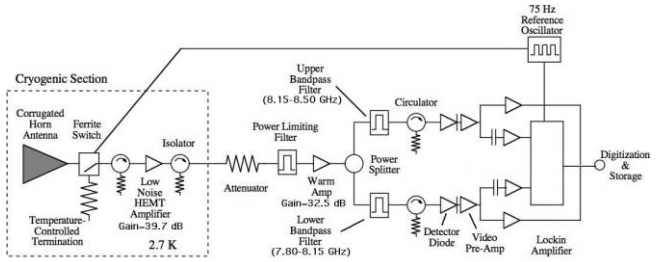

FIG. 2.—Schematic of the ARCADE 2 radiometer system.

open cryogenic aperture, with the aperture and all radiometrically active components kept nearly isothermal with the microwave sky. The apparatus is flown on a balloon to reduce atmospheric emission to negligible levels. The entire instrument is contained within a large (1.5 m diameter, 2.4 m tall) open-bucket liquid-helium dewar, with cold temperatures achieved and maintained through helium boil-off and a network of superfluid pumps. Any possible effects of frozen nitrogen, which can result from atmospheric condensation on the cold optics at balloon altitudes, are greatly reduced by using boiled-off helium gas to drive nitrogen away, with heating of the aperture available to sublimate frozen deposits.

Although designed as a doubly nulled instrument with an external calibrator, in the observations presented herein we were unable to use the external calibrator and instead operated as a singly nulled Dicke-switched radiometer, in which incident radiation is compared with a temperature-controlled internal reference load. Figure 2 shows the 8 GHz ARCADE 2 radiometer chain as flown.

The incident radiation from the sky is coupled to the radiometer through a corrugated feed horn antenna. The feed horn has an 11.6° full-width at half-power Gaussian beam and is mounted at an angle to point 30° from zenith. It is sliced at the aperture to be flush with the cold horizontal aperture plane. The 30° slice has a minimal effect on the symmetry of the beam (Singal et al. 2005).

Radiation coming in from the horn is compared with an internal reference load. At 8 GHz, the internal load is a wedge termination in waveguide with of a layer of Steelcast, a microwave absorber consisting of stainless steel powder mixed with a commercially available epoxy (Wollack et al. 2006a), cast onto an aluminum substrate. The load is highly isothermal, with thermometers cast into place to monitor the absorber temperature. It is sufficiently black and isothermal to be used as an absolute temperature standard, with measured return loss better than -35 dB across the entire frequency band at both room and cryogenic temperatures (Wollack et al. 2006b).

A ferrite waveguide switch chops between the horn and internal load at 75 Hz. The radiation is then amplified by a cold high electron mobility transistor (HEMT) amplifier and propagates in coaxial cable to a warm stage outside of the dewar. The cold amplifier has a gain of 39.7 dB and a system noise temperature of 11 K. The warm stage features a warm HEMT amplifier, a bandpass filter to select the desired frequency band, a second warm HEMT amplifier, and a power divider to split the signal into a high- and a low-frequency channel. Each of the two channels has a bandpass filter and a detector diode, followed by a video-frequency preamp, outputting a voltage level corresponding to the intensity of the radiation. The voltage signal is then processed by readout electronics that include a 75 Hz lock-in amplifier with adjustable gain that modulates the signal in phase with the waveguide switch, and an integrator that integrates the demodulated signal for a half-second. Finally, the signal is digitized and placed

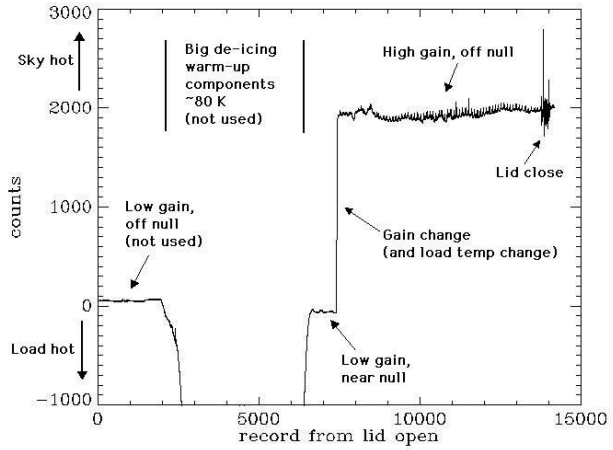

FIG. 3.—Time-ordered 8 GHz low-channel AC lockin output following the opening of the instrument lid. The spatial structure of the Galaxy is visible in the high-gain data.

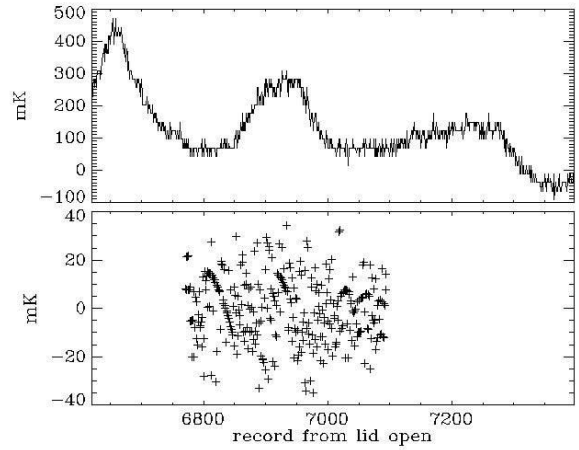

FIG. 4.—Time-ordered 8 GHz high-channel AC lockin output for the null period (*top*), and residuals of the least-squares fit for null data period with falling switch temperature (*bottom*). The dominant structure in the time-ordered data is caused by changes in the temperature of the internal load.

into the data stream, with each record of data corresponding to approximately 1 s and containing readings from all radiometer lockin outputs, thermometers, and onboard instruments.

All cryogenic temperatures are measured with ruthenium oxide resistance thermometers, which are read by a four-wire measurement with a 1 μA square-wave driving current (Fixsen et al. 2002). Resistance versus temperature curves for these thermometers have been determined by calibration against a National Institute of Standards and Technology standard, with the λ superfluid transition, clearly visible in the calibration data, used as an absolute in situ reference.

The dewar is suspended from a spreader bar supporting a V-shaped reflective shield designed to direct the edge of the antenna beams away from the flight train and balloon. A motor at the junction of the flight train and the cables holding the shield maintains the spinning of the dewar so that the antenna beams, pointing 30° from vertical, sweep out a circle on the sky 60° in diameter.

The external calibrator target resides on a rotating carousel structure atop the aperture plane, which can be turned to expose different feed horns to the sky or to the calibrator target. The hole for sky viewing has reflective stainless steel flares that shield the edges of the antenna beam from instrument contamination and that direct boiled-off helium gas out of the hole to discourage nitrogen condensation in the horn aperture.

3. OBSERVATIONS

The ARCADE 2 instrument was launched for its maiden flight on a 28 million cubic foot (790 Ml) balloon from the National Scientific Balloon Facility, which has since been renamed the Columbia Scientific Balloon Facility (CSBF), in Palestine, Texas, at 1:42 UT on 2005 July 29. Longitude, latitude, and altitude were determined throughout the flight with Global Positioning System (GPS) receivers provided by CSBF. The lid was opened for observation at 5:30 UT (0:30 local time) at a float altitude of 36 km. At this point, a gear failure prevented any movement of the carousel structure, freezing the instrument configuration in a position such that the 3 GHz horn was largely viewing the external calibrator target, the 8 GHz horn was viewing the sky, the 10, 30, and 90 GHz horns were completely obscured, and the 5 GHz horn was partially obscured. Thus, meaningful sky data were only available at 8 GHz.

In total, there are nearly 4 hr of flight observations with the instrument lid open, corresponding to 13,770 data records. The first half of this time was occupied with unsuccessful attempts to move the carousel, including a heating of the aperture plane to near 100 K and a subsequent slow cooling. With cryogenic temperatures then restored, there are 550 records with the lock-in amplifier's gain at the lowest setting and the internal load temperature controlled so that the radiometer was near null. A null condition is when the radiometer output is zero counts, corresponding to no temperature difference between the internal load and the object being viewed. Following that, the lockin gain was set to 16 times higher, and we simultaneously lost the ability to control the internal load temperature, with it dropping to the liquid helium bath temperature of $\sim$1.5 K. There then follow more than 6000 records of this high-gain data with the radiometer far from null. After this, the lid was closed and the flight was terminated at 10:10 UT. Figure 3 shows the 8 GHz low-channel radiometer output for records in which the lid was open.

The null data, from records 6771–7396, are useful because they are in the regime where the radiometer is insensitive to $1/f$ drifts in amplifier gain. However, because these data are at low lock-in gain, noise contributions from the lockin amplifier dominate the total noise, resulting in a relatively poor signal-to-noise ratio. Conversely, the high-gain data, from records 7397–13,769, are useful in that the spatial variation on the sky is very prominent; however, since the radiometer is far off of null, it shows large $1/f$ gain drifts. Figures 4 and 5 show the 8 GHz high-channel radiometer output for the null data and a representative sample of the high-gain data, respectively. A summary of the data used for analysis is presented in Table 1.

In all, 728 data records, or 10%, of the 6997 total for the combined null and high-gain period were excised from analysis. Thirty-nine data records were removed during the time when the internal load temperature was rapidly cooling to the bath temperature. Ninety-six records during an anomalous dip in the low-channel radiometer were removed, as were three sections of fewer than 20 records each corresponding to anomalous spikes in radiometer output. There were additional spikes in radiometer output that repeated over several rotations, consistent with a very warm object such as the Moon or Galactic center passing through the sidelobe of the antenna beam as reflected off of the reflective shield. These records were excised along with corresponding

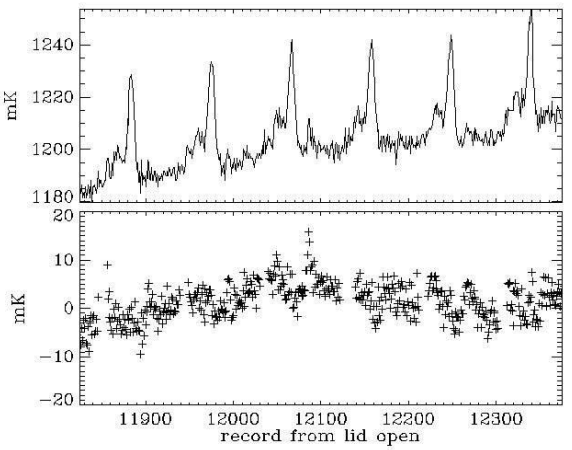

FIG. 5.—Time-ordered 8 GHz high-channel AC lockin output for records 11,825–12,375, a representative sample of the high-gain period (*top*), and residuals of the least-squares fit for those records (*bottom*). The Galactic signal and $1/f$ drift are clearly visible in the time-ordered data.

records at the same rotational phase for several periods before and after the spikes were visible in the time-ordered data, for a total of 513 records. An additional 18 records were removed for being single-point outliers, possibly as a result of transmission errors from the payload to the ground.

The ARCADE 2 instrument was equipped with a three-axis magnetometer to determine rotation about the vertical axis of the dewar by giving the orientation of the instrument relative to Earth's magnetic field. In addition, two clinometers were on board to measure the pitch and roll of the instrument. Figure 6 shows the portion of the sky viewed by the antenna beam during the records used for data analysis, in Galactic coordinates, on top of a *WMAP* 2003 K-band combined Galactic emission map. In order to reconstruct the pointing of the 8 GHz antenna beam on the sky, we first use the magnetometer data, and the latitude, longitude, and altitude data as provided by the onboard GPS, to determine the azimuthal rotation of the antenna beam about the axis of the dewar, assuming that the dewar is absolutely vertical. The latitude, longitude, and altitude data are used to calculate the direction of Earth's magnetic field at the position of the dewar in any given data frame by means of a routine utilizing International Geomagnetic Reference Field (IGRF) data, and the direction of this field as read by the magnetometer provides the orientation of the magnetometer and therefore the instrument in Earth-fixed coordinates. A simple coordinate rotation then can be used to transform the antenna beam from a dewar to a celestial coordinate system.

TABLE 1
SUMMARY OF DATA USED FOR ANALYSIS

Quantity	Null Data	High-Gain Data
System gain, low channel (counts K^{-1}).....	93.4	1487.3
System gain, high channel (counts K^{-1})	74.7	1189.3
Internal load temperature (K).....	2.473 to 2.718	1.446 to 1.460
White noise, low channel (mK $Hz^{-1/2}$)	9.0	2.1
White noise, high channel (mK $Hz^{-1/2}$)	9.3	2.1
$1/f$ knee, low channel (mHz).....	22	350
$1/f$ knee, high channel (mHz).....	18	400
Total records	625	6372
Number of excised records.....	29	700

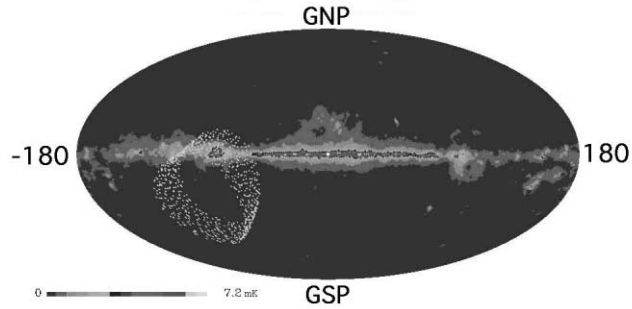

FIG. 6.—Portion of sky viewed during data records used for analysis, in Galactic coordinates, on top of a *WMAP* 2003 K-band combined Galactic emission map. The resolution is 0.9°. The position of the centroid of the antenna beam is sweeping out the circle shown clockwise, and drifting downward over time. Free-free emission is more heavily concentrated in the spiral arm viewed, while synchrotron emission is more diffuse throughout the Galactic plane.

We then check the pointing of the axis of the antenna beam by optimizing a simultaneous fit to template beam-smoothed maps of Galactic emission as outlined below, while allowing a parameter describing the pitch of the instrument to vary. We determined the pitch of the instrument to be a constant -2.2°, in agreement with the clinometer data.

4. ESTIMATION OF $T_{\rm CMB}$ AND GALACTIC EMISSION LEVELS

The output of the radiometer depends on radiometric temperatures on the sky and couplings to various temperatures within the system. In any given data record, we model the radiometer output in counts as

$$R = G(T_{\rm amp})[T_A(1-a) - bT_{\rm load} + aT_{\rm horn} + cT_{\rm switch}] + D,$$

where G is the system gain, the conversion factor between counts and temperature, which may be a function of the cold HEMT amplifier temperature $T_{\rm amp}$, T_A is the total antenna temperature of sources external to the horn aperture, $T_{\rm load}$ is the internal load temperature, $T_{\rm horn}$ is the temperature of the feed horn, a is the feed horn emissivity, $T_{\rm switch}$ is the temperature of the ferrite waveguide switch, and D is a constant offset signal generated by the lockin amplifier. The factors b and c are related to properties of the waveguide switch, as described below.

The antenna temperature T_A is itself a combination of the background CMB temperature $T_{\rm CMB}$, the small contribution from the instrument train and balloon $T_{\rm it}$, the antenna temperature of Galactic free-free and synchrotron emission, as well as that of the CMB dipole, convolved with the antenna beam. We can express it as

$$T_A(\boldsymbol{x}) = T_{\rm CMB} + T_{\rm ff}(\boldsymbol{x}) + T_{\rm synch}(\boldsymbol{x}) + T_{\rm dipole}(\boldsymbol{x}) + T_{\rm it},$$

where $\boldsymbol{x}$ is the direction vector to the point on the sky in question, $T_{\rm ff}$ and $T_{\rm synch}$ are the Galactic free-free and synchrotron emission signal and $T_{\rm dipole}$ is the temperature of the CMB dipole at the point on the sky in question, all three of which are spatially varying; $T_{\rm CMB}$ and $T_{\rm it}$ are spatially isotropic. We neglect the contribution to the antenna temperature from integrated extragalactic synchrotron emission, as this will be less than half a millikelvin at the frequency band in question (Reich et al. 2004). Given the $1/f$ drift in the high-gain data, we cannot reliably map the sky to millikelvin precision. We therefore model the sky as a superposition of monopole, dipole, and Galactic emission and fit

TABLE 2
Coefficients from the Least-Squares Fit: Low Channel

Parameter	Fit From[a]	Value from Fit	Statistical Uncertainty in Fited Value
System gain (G) (counts K^{-1})	N	93.4	0.7
Antenna emissivity (a)	N	0.006	0.001
System offset for nonnull (s)	N, H	−5.1	0.2
Multiple of model free-free map ($\alpha_{\rm ff}$)	N, H	0.69	0.02
Multiple of model synchrotron map ($\alpha_{\rm synch}$)	N, H	1.21	0.04

[a] (N) null data; (H) high-gain data.

to model parameters to obtain the best-fit Galactic and monopole components. We model

$$T_{\rm ff}(\boldsymbol{x}) + \alpha_{\rm ff} T_{\rm ff}^{\rm model}(\boldsymbol{x}),$$

$$T_{\rm synch}(\boldsymbol{x}) = \alpha_{\rm synch} T_{\rm synch}^{\rm model}(\boldsymbol{x}),$$

where $T_{\rm ff}^{\rm model}$ and $T_{\rm synch}^{\rm model}$ are template beam-smoothed maps of Galactic free-free and synchrotron emission, respectively.

The factors b and c are related to the asymmetry of the switch, specifically the different attenuation in each of the two arms. Unfortunately, the switch asymmetry in the flight configuration is not known. In addition, the switch and cold HEMT amplifier are isothermal as designed. Therefore, the switch coupling and temperature-dependent portion of the gain are highly degenerate and are also degenerate with other components having a similar temperature profile in time. These effects would cancel if the radiometer had viewed the external calibrator target as planned, but they are important for the singly nulled measurement reported here.

We therefore use the first 200 records of the null low-gain data, where the switch temperature is falling, to perform a simultaneous least-squares fit for G and a. Then, using the determined values of G and a as fixed inputs, both the null low-gain and off-null high-gain data are used to simultaneously fit for $\alpha_{\rm ff}$ and $\alpha_{\rm synch}$, as well as a parameter accounting for the offset difference in the system between the null and nonnull conditions (s). The values for $\alpha_{\rm ff}$ and $\alpha_{\rm synch}$ were then fed back and the 200 records of null low-gain data were again used to determine the best-fit G and a. All fit values converged by this second iteration. Figure 4 shows the residuals for the null period. We then attempted to quantify the effects of the switch and amplifier temperature as described in § 5.

We weight all data points with the inverse of the Gaussian noise variance. This results in the high-gain data having a factor of 4 larger weight. The results of the iterative least-squares fitting procedure are summarized in Tables 2 and 3. In addition to the parameters listed there, we determined that the radiometer had vanishingly small (sub-millikelvin) couplings to the payload altitude and various derivatives of temperatures, as expected, and a statistically insignificant coupling to both the aperture plane temperature and the temperature of the flares, in agreement with emission modeling.

During the time when the radiometer was off null, with the internal load more than 1 K colder than the sky, the radiometer output was subject to drifts due to $1/f$ gain fluctuations in the cold amplifier. Therefore, it was necessary, when fitting to the high-gain data, to use a high-pass filter on the data. To verify that this does not result in the loss of any sky signal, we generated simulated data sets with an input Galactic emission model and random realizations of $1/f$ noise and performed the simultaneous fit to the Galactic model with our high-pass filter in place. We were able, with two different input Galactic emission models and 1000 random realizations of $1/f$ noise each, to recover an average of 1.00 times the input Galactic signal with a standard deviation of 0.02.

4.1. *Galactic Emission Levels*

We model Galactic emission by interpolating between the 408 MHz full-sky survey (Haslam et al. 1982) and the *WMAP* data at 22 GHz (Bennett et al. 2003) to produce template maps of free-free and synchrotron emission at the ARCADE frequency bands. We produced a free-free map by scaling the *WMAP* first-year free-free map with a uniform spectral index of −2.1 and then smoothing with an 11.6° Gaussian. We produced a synchrotron map by first scaling the *WMAP* free-free map to 408 MHz with a spectral index of −2.1 and correcting the 408 MHz map for the scaled free-free emission. We then scaled the corrected map to the ARCADE frequency bands using a spectral index of −2.78, which is the mean spectral index between the corrected map at 408 MHz and the *WMAP* synchrotron map at 22 GHz. The scaled synchrotron map is then smoothed with an 11.6° Gaussian. The ARCADE 2 beams are sufficiently wide at 11.6° that the correction for the different beam widths of the *WMAP* K-band data and the Haslam 408 MHz data is negligible.

TABLE 3
Coefficients from the Least-Squares Fit: High Channel

Parameter	Fit From[a]	Value from Fit	Statistical Uncertainty in Fited Value
System gain (G) (counts K^{-1})	N	74.7	0.7
Antenna emissivity (a)	N	0.007	0.001
System offset for nonnull (s)	N, H	−4.6	0.2
Multiple of model free-free map ($\alpha_{\rm ff}$)	N, H	0.68	0.02
Multiple of model synchrotron map ($\alpha_{\rm synch}$)	N, H	0.93	0.05

[a] (N) null data; (H) high-gain data.

The *WMAP* data are differential and do not uniquely determine the zero level of free-free emission. Emission from the warm (electron temperature 10^4 K) component of the interstellar medium may also be traced by recombination lines in the ionized gas. Finkbeiner (2003) presents a full-sky map of Hα emission, for which the zero level is measured. We fix the zero level of the free-free map at 22 GHz by scaling the Hα zero level by a factor 11.4 uK R^{-1} as derived for the *WMAP* first-year data (Bennett et al. 2003).

We estimate the Galactic emission by fitting the free-free and synchrotron template maps to the ARCADE 2 sky data. The spatial structure is insensitive to the zero level of the template maps, although the zero level will affect the magnitude of the overall coupling. Extinction and scattering of Hα emission by interstellar dust complicate the comparison of Hα with free-free emission. This is negligible at the high latitudes used to fix the zero level. Dust extinction becomes significant in the Galactic plane, where direct comparison of free-free with Hα emission becomes problematic. For this reason, we use the *WMAP* maximum entropy model of the spatial distribution of free-free emission. This model combines microwave with Hα data such that the microwave data dominate in regions of high signal-to-noise ratio (e.g., the Galactic plane), while relaxing to the Hα prior in regions with poor signal-to-noise ratio. The overall accuracy of this model is estimated at a few percent of the total free-free emission (Bennett et al. 2003), which is sufficient. As the portion of the sky viewed was largely in the direction of the nadir of the CMB dipole, we use existing knowledge of the dipole as an input to the analysis.

As seen in Tables 2 and 3, we obtain $\alpha_{\rm ff} = 0.69 \pm 0.02$ and $\alpha_{\rm ff} = 0.68 \pm 0.02$ for the low and high channels, respectively, and $\alpha_{\rm synch} = 1.21 \pm 0.04$ and $\alpha_{\rm synch} = 0.93 \pm 0.05$. This means that we observe 69% as much free-free and approximately as much synchrotron signal as expected from the naive scaling described above. This corresponds, at an effective frequency of 8.15 GHz over the portion of the sky covered, to an observed 34 mK beam-smoothed peak signal for free-free emission in the Cygnus spiral arm, and an observed 19 mK beam-smoothed peak signal for synchrotron on the outer reaches of the Galactic bulge. For comparison, the naive extrapolation and interpolation would give an average of 50 mK beam-smoothed peak signal for free-free emission and a 17 mK signal for synchrotron in these directions. The data are consistent with the simple synchrotron model but prefer a modestly lower free-free signal in the spiral arm viewed.

An examination of the data and residuals, as in Figure 5, and a plot of the data and the best-fit Galactic model, as in Figure 7, shows that these amounts of Galactic coupling provide for the dominant spatial structure in the data. We repeated the fitting process with an alternate template synchrotron emission map generated by scaling the free-free–removed Haslam map by the spatially different spectral index determined by comparing this map and the *WMAP* K-band synchrotron emission map pixel by pixel. The coupling to this map was lower, at 0.42 for the low channel and 0.43 for the high channel, with a considerably lower significance.

We repeated the Galactic fitting with yet another template synchrotron emission map, one generated by removing a free-free signal from and isotropically scaling as above the 1420 MHz northern sky survey carried out by Reich and Reich (Reich 1982; Reich & Reich 1986). The coupling to this map, at 1.17 ± 0.01 for the low channel and 0.89 ± 0.01 for the high channel, is roughly similar to that of the free-free–removed isotropically scaled Haslam map, indicating both the consistency of the radio surveys and the repeatability of our analysis. We achieve a best-fit synchrotron spectral index from 408 MHz to 8.15 GHz of -2.6 ± 0.2 and a best-fit index from 1.42 GHz to 8.15 GHz of -2.7 ± 0.2.

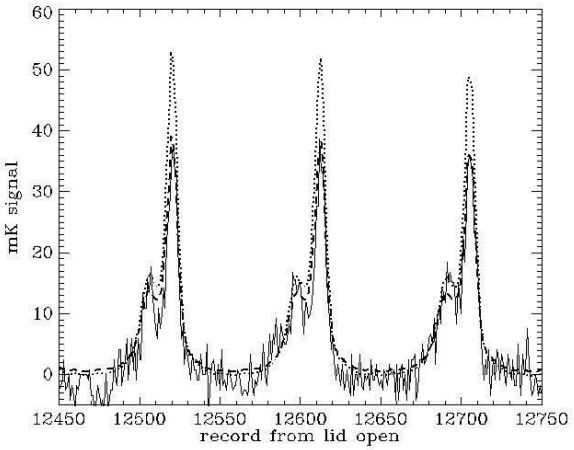

FIG. 7.—Plot showing time-ordered 8 GHz high-channel AC lockin output for records 12,450–12,750 (*solid line*), along with the best-fit model from the least-squares fit (*dashed line*) and a model with $\alpha_{\rm ff} = \alpha_{\rm synch} = 1$ (*dotted line*).

Finally, we repeated the Galactic analysis with cuts of the data, including cutting various sections of the data records, and cutting records from Galactic latitudes greater or less than 15° from the Galactic equator. Removing sections of data records and removing Galactic latitudes more than 15° from the Galactic equator yielded results consistent with the above analysis. Removing Galactic latitudes within 15° of the Galactic equator leads to greatly inflated statistical error bars, such as to render the free-free fit insignificant. This is as expected, as the spatial structure lies almost entirely within the plane of the Galaxy.

4.2. *Estimation of* $T_{\rm CMB}$

The CMB temperature ($T_{\rm CMB}$) and the antenna temperature of emission from the instrument train and balloon ($T_{\rm it}$) in combination constitute the spatially isotropic "monopole" portion of the sky signal. The monopole temperature was determined, using a period of the null data where the switch temperature was more steady, by performing a linear fit of the load temperature to the radiometer output with the back-end offset (D) and the couplings to the horn temperature (a) and the template Galactic emission maps, which include a Galactic zero level, subtracted out, to obtain the load temperature at which the radiometer output was zero counts. This is then the monopole temperature. The relative magnitude of the swing in the switch temperature during its fall and the residuals from those records can then be used to quantify the uncertainty due to switch and amplifier temperature effects.

The constant offset in the radiometer generated by the lockin amplifier was measured in ground testing many times and in the flight configuration prior to launch and was shown to vary between -75 and -80 counts in the 8 GHz low channel and between -110 and -100 counts in the high channel. We estimate the magnitude of this offset during the null data period of the flight by comparing the radiometer output just prior to, and just after, the gain change. We determine that the offset during flight is -77.5 ± 0.6 counts in the low channel and -102.1 ± 0.3 counts in the high channel.

Figure 8 shows a plot of the high-channel AC lockin output with the horn, Galactic, and back-end offset contributions taken out versus the internal load temperature during the null records for which the switch temperature was steadiest. The monopole

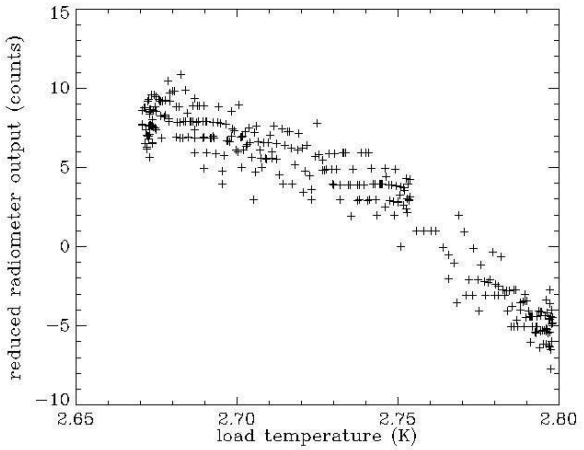

FIG. 8.—Plot of high-channel AC lockin output with horn, Galactic contribution, and back-end offset taken out vs. internal load temperature, for null records 7095–7397, during which the switch temperature was steadiest. The monopole temperature is the load temperature where the radiometer is exactly nulled, i.e., where this reduced radiometer output is zero counts.

temperature is the load temperature at which this reduced radiometer output is zero counts.

To derive T_{CMB} from the measured monopole temperature, we must model and subtract the emission and reflection contributions from the flares, the reflective shield, and parts of the flight train visible at the edges of the antenna beams, including a piece of the balloon, a camera, lights, a bar at the bottom of the shield from which the dewar hangs, and the cables connecting the dewar to this bar. To model the antenna temperature contribution from each component, we assume that the object is both emitting and reflecting the warm ground. We assign a reflectivity and an emissivity, assume the temperature of the object to be 250 K and that of the ground to be 300 K, and then convolve the object with the antenna beam. The largest contribution is from the shield, which, as a smooth aluminum surface, we model with an emissivity of 0.005 and a glint-to-ground power reflection of 0.001. The reflected ground component is small, and tip scans with the previous-generation ARCADE instrument (Fixsen et al. 2004) verified this emisssivity to be accurate within 30%. We repeat the calculation with the shield suspension angle varying $\pm 2.5^{\circ}$ and the emissivity to varying up to 30% to give a shield antenna temperature contribution of 8 ± 4 mK. The contribution from the other components totals 2.2 mK, to which we can assign an uncertainty of 30%, or 0.7 mK. With the instrument emission subtracted from T_{mono}, we determine a value for T_{CMB} of 2.766 K at 8.3 GHz and 2.897 at 8.0 GHz.

5. UNCERTAINTY ESTIMATES

The raw statistical uncertainty in the values for the T_{CMB} and the Galactic map multipliers were determined from the least-squares fit. In addition, the value of T_{CMB} is subject to significant sources of systematic uncertainty, described below. We add the statistical and systematic sources of uncertainly in quadrature to determine a total uncertainty of ± 116 mK in the low channel and ± 160 mK in the high channel. An uncertainty summary for T_{CMB} is presented in Table 4.

The dominant source of uncertainty in the values for T_{CMB} arises from the unknown coupling of the amplifier and switch temperatures to the radiometer output. We conservatively bound this effect by comparing the residuals of the least-squares fit during the 200 records of the null data where the switch temperature was falling to the change in the switch temperature. We divide the standard deviation of the residuals of these records by the total swing in the switch temperature during the period to obtain an estimate for the factor by which the switch temperature is to be multiplied to cause a 1 σ swing in the monopole level. This factor is 0.08 for the low and 0.11 for the high band. The steady switch temperature of 1.455 K during the records where the monopole temperature was determined is then multiplied by this factor to obtain an upper limit uncertainty due to switch and amplifier temperature effects of ± 116 mK in the low band and ± 160 mK in the high band.

Other contributions to the error budget are small. Uncertainty in the antenna emissivity will contribute to uncertainty in the monopole temperature. To estimate the effect on the monopole temperature, we propagate this uncertainty, leading to a value of ± 6 mK for the monopole level in both the high and low channels. The corresponding changes in the values for the Galactic map multipliers are an order of magnitude below the level of their statistical uncertainty and are consequently ignored.

Another potential source of systematic errors is thermometry. By observing the λ superfluid transition in thermometer calibration and flight data, we can bound thermometry errors in flight to less than ± 3 mK. To first order, this is only relevant in the monopole value. Higher order effects, which could arise because of the nonlinearity of the thermometer temperature resistance curves, are negligible.

TABLE 4
SUMMARY OF UNCERTAINTIES FOR T_{CMB}

	Low Channel (mK)		High Channel (mK)	
Source	Size of Effect	Uncertainty Contribution	Size of Effect	Uncertainty Contribution
Statistical uncertainty	...	3	...	1
Switch temperature effects	...	116	...	160
Radiometer back-end offset	812	6	1369	3
Antenna emissivity	19	6	13	6
Shield emission	8	4	8	4
Other flight-train components	2	1	2	1
Thermometry	...	3	...	3
Galactic zero level	4	1	4	1
Total uncertainty		116		160

NOTES.—Uncertainty estimates are discussed in § 5. Uncertainties are added in quadrature. Employment of the external calibrator in future flights will eliminate the contributions from the switch-temperature effects and the antenna emissivity.

There are three sources of systematic uncertainty in the measured value of $T_{\rm CMB}$ that are irrelevant in the determination of the Galactic map multipliers. These are uncertainties in level of constant offset in the radiometer generated by the lockin amplifier, in the determination of flight-train emission, and in the zero level of Galactic emission. The first two effects were discussed and their uncertainties quantified in § 4.2. Our uncertainty in the zero level of Galactic emission at 8.0 and 8.3 GHz springs from a combination of the uncertainty in the zero level of our input foreground maps, which were then interpolated, and the change in zero level between the different model synchrotron maps considered. The uncertainty in the zero level of synchrotron emission due to the uncertainty in $\alpha_{\rm synch}$ is less than 1 mK. We observe a 1 mK difference in the zero level of synchrotron emission between the model synchrotron emission maps considered. The uncertainty in the zero level of the Haslam map at 408 MHz is reported as ± 3 K (Haslam et al. 1982), which, scaled by a -2.8 spectral index to 8.0 and 8.3 GHz, corresponds to ± 1 mK. We thus report a ± 1 mK uncertainty due to the Galactic zero level.

The level of uncertainty in the Galactic map multipliers due to all of the systematic effects considered is well below their raw statistical uncertainty, as is the effect on their value of the system gain uncertainty. Thus, we report uncertainties of 0.02 for $\alpha_{\rm ff}$ and 0.04 for $\alpha_{\rm synch}$ at 8.0 GHz and 0.02 for $\alpha_{\rm ff}$ and 0.05 for $\alpha_{\rm synch}$ at 8.3 GHz.

6. DISCUSSION

We report $T_{\rm CMB}$ to be 2.897 ± 0.116 K at 8.0 GHz and 2.766 ± 0.160 K at 8.3 GHz. These measurements are consistent with FIRAS at higher frequencies and ground-based measurements at lower frequencies.

We have fitted the spatial structure in the time-ordered data to template free-free and synchrotron emission maps generated by scaling 2003 *WMAP* K-band and Haslam 408 MHz sky survey data. We recover a mean best-fit synchrotron amplitude of 1.07 ± 0.05 times the template map, corresponding at an effective frequency of 8.15 GHz to a physical peak signal height on the outer reaches of the Galactic bulge of 19 mK after the signal is convolved with the 11.6° antenna beam. This implies a best-fit synchrotron spectral index from 408 MHz to 8.15 GHz of -2.6 ± 0.2.

We recover a best-fit free-free emission amplitude of 0.69 ± 0.02 times the template map, corresponding at an effective frequency of 8.15 GHz to a peak signal height in the Cygnus spiral arm viewed of 34 mK when the signal is convolved with the antenna beam. Recent *WMAP* 3 year results state a lower conversion of 8 μK R^{-1} between Hα intensity and free-free emission temperature (Hinshaw et al. 2006), consistent with the free-free emission intensity we obtain, which is 70% as high as the *WMAP* first-year result.

We demonstrate repeatability of the Galactic analysis by substituting the Reichs' 1420 MHz northern sky data for the Haslam data. The difference in $\alpha_{\rm synch}$ between the low and high channels is present with both Reich and Haslam data as inputs to the template map, which points to this being related to the more diffuse nature of the synchrotron signal relative to the free-free signal in the region of the Galaxy observed. With the synchrotron signal less sharply peaked, it is much more susceptible to confusion with residual $1/f$ noise in the data.

ARCADE 2 is scheduled to fly again in 2006 with a redesigned carousel movement mechanism. With the sky compared with the external calibrator, switch and amplifier temperature issues and $1/f$ drifts will be irrelevant to first order, and a much more precise value for $T_{\rm CMB}$ will be achieved at frequencies ranging from 3 to 90 GHz. In addition, with $1/f$ drifts irrelevant, we will be able to produce from scratch Galactic emission intensity maps.

This work was supported by NASA's Science Mission Directorate under the suborbital program RTOP 188-02-54-01. We thank the staff at CSBF for launch support. We thank Victor Kulesh for contributions to the ground software, and Adam Bushmaker, Jane Cornett, Paul Cursey, Luke Lowe, Sarah Fixsen, and Alexandre Rischard for their work on the project. We acknowledge the use of the Legacy Archive for Microwave Background Data Analysis (LAMBDA). Support for LAMBDA is provided by the NASA Office of Space Science. The research described in this paper was performed in part at the Jet Propulsion Laboratory, California Institute of Technology, under a contract with the National Aeronautics and Space Administration.

REFERENCES

Bartlett, J. G., & Stebbins, A. 1991, ApJ, 371, 8
Bennett, C. L., et al. 2003, ApJS, 148, 97
Bersanelli, M., Bensadoun, M., De Amici, G., Levin, S., Limon, M., Smoot, G. F., & Vinje, W. 1994, ApJ, 424, 517
Burigana, C., Danese, L., & De Zotti, G. 1991, A&A, 246, 49
Draine, B. T., & Lazarian, A. 1998, ApJ, 494, L19
Finkbeiner, D. P. 2003, ApJS, 146, 407
Fixsen, D. J., Cheng, E. S., Gales, J. M., Mather, J. C., Shafer, R. A., & Wright, E. L. 1996, ApJ, 473, 576
Fixsen, D. J., Kogut, A., Levin, S., Limon, M., Lubin, P., Mirel, P., Seiffert, M., & Wollack, E. 2004, ApJ, 612, 86
Fixsen, D. J., Mirel, P., Kogut, A., & Seiffert, M. 2002, Rev. Sci. Instrum., 73, 3659
Fixsen, D. J., Wollack, E., Kogut, A., Limon, M., Mirel, P., Singal, J., & Fixsen, S. M. 2006, Rev. Sci. Instrum., 77, No. 064905
Haslam, C. G. T., Salter, C. J., Stoffel, H., & Wilson, W. E. 1982, A&AS, 47, 1
Hinshaw, G., et al. 2006, ApJ, submitted (astro-ph/0603451)
Jonas, J. L., Baart, E. A., & Nicolson, G. D. 1998, MNRAS, 297, 977
Platania, P., Bensadoun, M., Bersanelli, M., De Amici, G., Kogut, A., Levin, S., Maino, D., & Smoot, G. F. 1998, ApJ, 505, 473
Reich, P., & Reich, W. 1986, A&AS, 63, 205
———. 1988, A&AS, 74, 7
Reich, P., Reich, W., & Testori, J. C. 2004, in The Magnetized Interstellar Medium, ed. B. Uyan\imathker, W. Reich, & R. Wielebinski (Katlenburg-Lindau: Copernicus), 63
Reich, P., Testori, J. C., & Reich, W. 2001, A&A, 376, 861
Reich, W. 1982, A&AS, 48, 219
Singal, J., Wollack, E., Kogut, A., Limon, M., Lubin, P., Mirel, P., & Seiffert, M. 2005, Rev. Sci. Instrum., 76, No. 124703
Wollack, E. J., Fixsen, D. J., Henry, R., Kogut, A., Limon, M., & Mirel, P. 2006a, Appl. Opt., submitted
Wollack, E. J., Fixsen, D. J., Kogut, A., Limon, M., Mirel, P., & Singal, J. 2006b, IEEE Trans. Instrum. Meas., submitted
Zel'dovich, Ya. B., & Sunyaev, R. A. 1969, Ap&SS, 4, 301